

Source related variations of strong ground motions in 3D: Application to the Newport-Inglewood Fault, Los Angeles Basin

Haijiang Wang*, Heiner Igel*, Frantisek Gallovic*, Alain Cochard*, Michael Ewald*

Department of Earth and Environmental Sciences, Ludwig-Maximilians-University of Munich, Theresienstraße 41, D-80333 Munich, Germany

Version 1.3, June 4, 2007.

Deterministic earthquake scenario simulations are playing an increasingly important role in seismic hazard and risk estimation. The numerical calculation of the complete 3D wavefield for a seismically active basin remains a computationally expensive task. Our aim is to provide a tool with which we can calculate a large number of different finite-source scenarios for a particular fault or fault system. In order to avoid having to run the expensive 3D code for each kinematic source description we propose the concept of "numerical Green's functions" (NGF): a large seismic fault is divided into sub-faults of appropriate size for which synthetic Green's functions at the surface are calculated and stored. Consequently, ground motions from arbitrary kinematic sources can be simulated for the whole fault or parts of it by superposition. The study area is a simplified, vertical model of the Newport-Inglewood (NI) fault in the Los Angeles (LA) Basin. After investigating the accuracy of the method for homogeneous and 3D media, the variations of surface ground motion (e.g., peak ground velocity and synthetic seismograms) related to the source complexity (e.g., hypocentre location and corresponding slip history) is estimated to demonstrate the functionality of the method. The results show a complex behavior, with

dependence of absolute PGV and its variation on asperity location, source directivity and local structure. Hypocentral depth may affect PGV in a positive or negative way depending on the distance from the fault and the location with respect to basin structure.

1. Introduction

The calculation of the complete wave-field for potential large earthquakes in a given seismically active region of known structure will play a central role in reliably estimating shaking hazard (e.g., Olsen and Archuleta, 1996; Olsen, 2000, Ewald *et al.*, 2006). Such calculations will complement hazard estimation based on probabilistic estimates of seismicity (e.g., Gerstenberger *et al.*, 2005) and/or stochastic means to calculate ground motion scenarios based on highly simplified physical models (e.g., Beresnev *et al.*, 1998; Boore, 2003). Earthquake-induced ground motions strongly depend on: (1) the velocity structure and (2) the finite-fault slip histories. The local and regional velocity structure can be estimated and continuously improved using tomographic tools and/or direct measurements (e.g., borehole information). However, the uncertainty concerning rupture processes (stress drop, source mechanisms, rupture velocity, slip speed, etc.) remains.

This poses a formidable problem when facing the task of estimating ground motion due to one or more “characteristic earthquakes” of a specific seismically active region. In addition to the uncertainties caused by the shallow velocity structure at frequencies relevant to structures, one would have to calculate many different slip scenarios for one presumed earthquake in order to account for rupture related variations. However, the numerical calculation of the complete 3D wavefield in the observed frequency band for a seismically active basin remains a computationally expensive task. This expense restricts seismologists either to calculating source

models with homogeneous media (e.g., Gallovic and Brokešová, 2004, 2007a, 2007b), or to calculating single source scenarios in 3D media (e.g., Olsen and Archuleta, 1996; Olsen, 2000; Ewald *et al.*, 2006).

In order to quantify these variations without running the expensive 3D code for each kinematic source scenario, we propose to generate data bases with Green's functions calculated for discrete models of faults or fault systems for areas with sufficiently well known 3D velocity structure and fault locations. The surface ground motions for each sub-fault excitation are stored which allows arbitrary finite-fault scenarios to be synthesized at very little computational cost compared to a normal complete 3D calculation once the database is available. The opportunity to investigate ground motion variations as a function of many different rupture related parameters for a specific area comes at the price of a sufficiently large number of initial 3D simulations for the pre-designed discretized fault and is economical only if the number of synthesizations exceeds the number of NGF calculations.

Similarly, Graves and Wald (2001) calculated a database of Green's functions. They put the source (double couple point source) at a station and record the response at the whole 3D grid. Those responses can, reciprocally, be used as Green's functions. Their work focuses on a few stations on the surface where ground motions are available, while the fault discretization can reach the same scale of the grid-length adopted by the numerical method. Whereas we are interested in providing the spatial map of the ground motion variation. We will calculate the ground response at each station of the study area but with an appropriate discretization of the fault plane.

In this paper we introduce the concept of the NGF method, discuss the accuracy of the method as a function of sub-fault size and other earthquake related parameters, and present a first application to a model of the Newport-Inglewood fault in the Los

Angeles basin, namely how the ground motion varies with the hypocentre location while final slip is unchanged. The method for calculating the quasi-dynamic rupture process published in Guatteri *et al.* (2004) is adopted to generate slip history based on randomly pre-created final slip distributions. This initial study merely aims at discussing the potential functionalities of this approach with restrictions in terms of lowest model velocities and achievable frequencies and is not “economical” in the sense described above.

2. Numerical Green’s Functions: Theory and Verification

In the following we introduce the basic concept of the NGF approach and verify it against high-resolution (“continuous”) finite-fault solutions. A target fault plane is divided into equally sized, rectangular sub-faults and for each of these sub-faults the corresponding Green’s function is calculated using a double-couple source mechanism (here we restrict ourselves to pure strike-slip excitation). Even though in a strict mathematical sense the term *Green’s function* is not correct we use it in connection with our source time function (a Delta function in moment rate) and to remark the relation to the concept of *empirical Green’s functions* (e.g., Joyner and Boore, 1986; Hutchings and Wu, 1990; Bour and Cara, 1997; Kohrs-Sansorny *et al.*, 2005). The calculations can be carried out using any numerical solution to the 3D wave propagation problem. Here we employ a high-order staggered-grid finite-difference approach (e.g., Igel *et al.*, 1995; Gottschämmer and Olsen, 2001) with efficient absorbing boundaries based on the concept of perfectly matched layers (e.g., Collino and Tsogka, 2001; Marcinkovich and Olsen, 2003).

Theory and verification

Following Aki and Richards (2002), the Green's function, $G_{ip}(x, t, \xi)$, is defined as the i -th component of the ground velocity response at position x and time t excited by a force impulse precisely located at ξ (unit amplitude and in p -direction). The wave field introduced by a pure shear fault, Σ , embedded in an isotropic medium is described by the representation theorem (Aki and Richards, 2002, equation 3.18) as:

$$v_i(x, t) = \iint_{\Sigma} s_r(\xi, t) \cdot \mu(\xi) \cdot \tilde{M}_{pq}(\xi) * \frac{\partial G_{ip}(x, t, \xi)}{\partial \xi_p} d\Sigma, \quad (1)$$

where $v_i(x, t)$ is the i th component of velocity at position x and time t . Scalar function $s_r(\xi, t)$ is the slip rate function located at ξ on the fault plane. Parameter $\mu(\xi)$ is the shear modulus of the medium. $\tilde{M}_{pq}(\xi) = u_p(\xi)n_q(\xi) + u_q(\xi)n_p(\xi)$ where $u(\xi)$ is the unit normal to the fault and $n(\xi)$ indicates the slip (rate) direction. The fault plane, Σ , can be divided into elements, σ_n ($n = 1, \dots, N$) and equation (1) is then reformulated as:

$$v_i(x, t) = \sum_{n=1}^N \iint_{\sigma_n} s_r(\xi, t) \cdot \mu(\xi) \cdot \tilde{M}_{pq}(\xi) * \frac{\partial G_{ip}(x, t - \tau(\xi), \xi)}{\partial \xi_p} d\sigma, \quad (2)$$

where the time term $\tau(\xi)$ is introduced to describe the time delay due to the rupture front propagation from the hypocentre to point ξ . Assume that σ_n is small enough and the difference between the individual $s_r(\xi, t)$, $\mu(\xi)$, $\tilde{M}_{pq}(\xi)$ and $\tau(\xi)$ can be neglected. We name the approximate variables as $s_r^n(t)$, μ^n , \tilde{M}_{pq}^n and τ^n . After moving them outside the integration in equation (2), we approximate equation (2) as:

$$v_i(x, t) \cong \sum_{n=1}^N \left(\tilde{M}_{pq}^n \cdot \iint_{\sigma_n} \frac{\partial G_{ip}(x, t - \tau^n, \xi)}{\partial \xi_p} d\sigma \right) * s_r^n(t) \cdot \mu^n. \quad (3)$$

Assuming constant Green's function $G_{ip,q}^n(x, t - \tau^n)$ (comma stands for the space derivative) inside a subfault n , we obtain

$$v_i(x, t) \cong \sum_{n=1}^N \left(\tilde{M}_{pq}^n \cdot G_{ip,q}^n(x, t - \tau^n) \right) * s_r^n(t) \cdot \mu^n \cdot A^n, \quad (4)$$

where A^n is the area of the n th small source σ_n . We name the part enclosed in the brackets as Numerical Green's function, $g_i^n(x, t - \tau^n)$, which can be calculated using a slip rate impulse with pre-chosen direction and fault geometry parameters. We obtain the basic equation for the synthesis of ground motions:

$$v_i(x, t) \cong \sum_{n=1}^N g_i^n(x, t - \tau^n) * s_r^n(t) \cdot \mu^n \cdot A^n. \quad (5)$$

Optimal subfault size - homogeneous model

Considering that the goal of the NGF method is to be able to synthesize - within some limits (e.g., reliable frequency range) - complete ground motions from arbitrary finite-source scenarios on a discretized fault, and that the generation of a NGF data base is computationally expensive, one should attempt to find a minimum number of sub-faults necessary to determine the ground motion with sufficient accuracy for a specific earthquake magnitude. It is instructive to analyze where possible errors are introduced when using a point source to represent a small source with certain size. Some approximations are made from equation (2) to equation (4). First, $s_r(\xi, t)$ is assumed to be the same which means each point inside one small source is assumed to rupture at the same time, and follow the same slip rate function. Secondly, each point inside the small source is assumed to rupture with the same source mechanism (identical $\tilde{M}_{pq}(\xi)$ across the subfault). Finally, the Green's functions are assumed to be the same inside σ_n . For our case - vertical fault plane, pure strike slip and

homogeneous medium across the fault plane - only the first and the fourth assumptions should be considered. The *optimal* (largest) size of such sub-faults is expected to depend on (1) the properties of the ruptures themselves (rupture speed, slip velocity, rise time etc.), (2) the position of the receiver relative to the rupture propagation (directivity which is a space function of the hypocentre location in strike and dip direction) and (3) the desired frequency band for the synthesized ground motions (i.e., the shortest wavelengths to be described in the 3D velocity model). This dependency is thoroughly investigated for a homogeneous medium (with parameters shown in table 1).

At first, seismic motions from a set of double-couple point sources at different depths, 1 km from each other, are calculated and stored (Fig. 1 top, solid circles). The seismograms recorded at the surface can be used as Numerical Green's functions. With appropriate horizontal space shifting, due to 1D symmetry of the medium, Numerical Green's functions corresponding to a planar vertical fault (Fig. 1 top, hollow circles) can be acquired for a given station, and finally synthesized to calculate the ground motions for a large earthquake. The parameters for one kinematic rupture test case are defined in the following way. The fault dimension of an Mw 7 earthquake is first chosen as 36x24 km (which can be evenly sub-divided into sub-faults of size 2x2, 3x3 and 4x4 km) and posed such that the strike direction is parallel to the x-axis of the study area. The top of the fault plane is set to be 1 km from the free surface (Fig. 1 top) and the two different hypocentres, G1 and G2, are located at the red asterisks (Fig. 1 bottom). The rupture propagates circularly from the hypocentre to the other parts of the fault plane with a constant velocity (Table 1). The scalar moment M_0 is related to the moment magnitude Mw as $\log M_0 = 1.5M_w + 16.05$ (Kanamori, 1977). The final average slip D is calculated as $D=M_0/(\mu A)$. A Gaussian static slip distribution is adopted with the half-widths in the strike and the dip direction chosen to be 17.2 and 5.8 km, respectively. The slip-rate function for each sub-fault in the time domain is

assumed to be a ramp function. The corresponding rise time is calculated as the ratio between the local static slip and the presumed constant slip velocity (Table 1).

The solution with sub-fault size of 1×1 km is first calculated and used as the “*continuous*” solution (Hutchings and Wu, 1990). Fig. 2a (top left corner) shows two seismograms from different solutions as an example. The misfit energy (ME) between the seismograms from the differently discretized solutions, i.e., sub-faults with side-length of 2.0 km, 3.0 km and 4.0 km, respectively, and the “*continuous*” solution, is used to measure the accuracy of the discretized solutions:

$$ME = \frac{\sum_{i=1}^{nt} (v_c(i\Delta t) - v_d(i\Delta t))^2}{\sum_{i=1}^{nt} (v_c(i\Delta t))^2} \times 100 \quad (6)$$

where $v_c(i\Delta t)$ is the “*continuous*” solution’s velocity and $v_d(i\Delta t)$ is the discretized solution’s velocity at time $i\Delta t$, respectively, Δt is the time step.

First, in Fig. 2a, the ME distribution on the surface between the solution of 4.0 km and the “*continuous*” solution is shown to exhibit the directivity effect on the accuracy for this Mw 7 earthquake. The y-component is used for this verification because it has larger ME in most of the working area than the other two components (Wang, 2007). In the triangle area in the opposite direction to the rupture propagation, the ME values are getting larger. But the largest ME with maximum value of 6.2% is found right on the fault projection.

Two hypocentres, different in depth (G1 and G2 in Fig. 1), are taken into account and synthesized with different size of sub-faults. The largest misfit-energy between the solutions of 2x2, 3x3 and 4x4 km and the “*continuous*” of the entire study area are shown in Fig. 2b as a function of hypocentre depth. When the hypocentre is

deeper, the ME gets smaller. Thirdly, the resulting seismic motions are low-pass filtered (Gaussian function) with different cut-off periods to investigate the frequency dependence of the accuracy. The largest ME values (over the whole study area) are shown in Fig. 2c as a function of the cut-off period. When the seismograms are filtered with cut-off period of 4.0 sec, the maximum ME values are smaller than those filtered with cut-off period of 3.0 sec, for the differently discretized solutions, respectively. Finally, six Mw 7 earthquakes (two different rupture velocities times three different sub-fault sizes) are simulated and the resulting largest ME values of the study area are shown in Fig. 2d as function of rupture velocity, from which we conclude that the accuracy increases with the rupture velocity.

3. Study area and NGF data base

We apply the NGF method to the Newport Inglewood (NI) fault system located in the Los Angeles basin (Fig. 3). An area of $96 \times 87 \times 25.5$ km, in the two horizontal and vertical directions, is selected as study area, and rotated in order to have one horizontal grid axis parallel to the NI fault. The velocity model is based on the elastic part of the SCEC 3D velocity model for the Los Angeles (LA) basin (Version 3, Kohler *et al.*, 2003). The depth of a shear wave velocity isosurface, 2.0 km/s, is shown in Fig. 4. The NI fault is chosen for several reasons: it hosted the M6.4 Long Beach earthquake in 1933 (Hauksson and Gross, 1991), causing serious damage; it is still considered the most probable source for a damaging earthquake to the LA area; the near-vertical plane can be approximated by a vertical plane to first order in the numerical calculation and the predominant right-lateral slip can be approximated with a pure strike-slip mechanism (Grant and Shearer, 2004). The main goal of the current study is to demonstrate the NGF concept and its functionalities. To reduce the computational effort and the size of the data base we truncate the seismic velocities at 1.4 km/s.

The accuracy of the synthesized ground motions as a function of sub-fault size is investigated for an Mw 7 earthquake with the computational setup and source parameters given in Table 2. The fault length L and width W are chosen to be 36 km and 18 km, respectively. Thus, the final fault geometry will be 120×60 (in grid points), which can be divided into sub-faults with size of 3×3, 4×4, 5×5 and 6×6 (in grid points). The method published in Guatteri *et al.* (2004) is adopted to produce the finite-fault scenario for an Mw 7 earthquake. This method is capable of accounting for the accelerating tendency of the crack front due to dynamic loading and the high stress-drop promotion of fast rupture propagation. The quasi-dynamic rupture process calculation starts with a 2D Gaussian auto-correlation function (isotropic correlation-length of 5 km). The shear-modulus on the fault is kept constant and corresponds to a shear velocity of 3.2 km/s. The final slip distribution is shown in Fig. 3 (top right corner). The resulting finite source scenario is simulated with three different equilateral sub-faults of side-length 0.3 km (treated as the “*continuous*” solution, corresponding to the finest grid distance), 1.5 km, and 1.8 km. The ground motions for the latter two sub-fault sizes are compared to those for the “*continuous*” solution.

As an indicator of the accuracy we compare the peak ground velocity (PGV) over the whole study area covering frequencies up to 0.5 Hz. This choice is somewhat arbitrary and other wave-field characteristics could be used (e.g., shaking duration, or a misfit criterion w.r.t. the “*continuous*” solution). Our specific goal here is to demonstrate that hazard-relevant variations due to finite-source scenarios can be efficiently carried out using the NGF methodology.

In Fig. 5a the relative PGV difference, i.e., ratio of the PGV difference (x-component) between one discretized solution (sub-fault size of 1.8 km) and the “*continuous*” solution divided by PGV of the “*continuous*” solution is shown. Large values are found to happen inside the basin. The largest relative PGV difference is

9.9% in the position of PGV 0.838 m/s (with an absolute PGV difference of 0.083 m/s). The waveforms from different solutions are almost identical in the profile shown in Fig. 5c with lowest peak correlation coefficient value of 0.988. This can also be seen from the waveform comparison (Fig. 5b) for one single station where the biggest PGV difference is observed (point P1, Fig. 5a). The maximum amplitude difference between the solution for 1.5 km sub-fault side-length and the “*continuous*” one is 0.039 m/s (4.6% in percentage). We consider this level of accuracy is enough for our case. To be on the safe side, we chose the sub-fault size (1.5 km) for the generation of the NGF data base.

The conclusion about the trend of the accuracy as a function of cut-off frequency (as shown for the homogeneous case) still holds in the 3D heterogeneous case. These results justify the choice of the final parameter setup used to calculate a complete set of NGFs for M7 earthquakes on the NI fault estimated to cover an area of $69 \times 20 \text{ km}^2$ (Jennings, 1994). As we primarily focus on differential effects we calculate a fault area of 40 (along strike) \times 13 (along depth) ($60 \times 19.5 \text{ km}^2$ from the north west edge of the NI fault) sub-fault NGFs (side length 1.5km) for a grid spacing of 300 m and seismograms up to 0.5 Hz. This fault area is already capable to cover the historical M6.4 Long Beach earthquake. The complete NGF data base includes the seismograms for the 140×166 equally spaced surface grid at 600 m distance, for 6 motion components (three translations and three rotations).

4. Source-related inter-event variations of 3D ground motions: effect of hypocentre location

The NGF data base calculated allows us - within the limits of the method (e.g., reliable frequency range) - to synthesize ground motions from arbitrary strike-slip histories on the NI fault for the complete study area. A question of considerable

practical relevance to estimates of seismic hazard is how variations of the hypocentre location for a given final slip distribution influence the shaking for a *characteristic* earthquake of a given magnitude. Amongst many other possibilities, this is the question we will focus on in this sample study: we assume the existence of a *characteristic* M7 earthquake on the NI fault section from the north-west fault edge and synthesize ground motions for a 4x6 regular grid of hypocentre locations in the seismogenic zone (5 - 15 km depth) as indicated in Fig. 3 (inlet). The same process as in the former section is adopted to produce the needed quasi-dynamic rupture processes, with varying hypocenter at this time.

Snapshots and profile:

In Fig. 6, snapshots of the y-component velocity on the surface are shown. Source and basin related effects on ground motion are recognized in this figure. Most energy is radiated to the area right of the fault plane due to the unilateral rupture propagation from left to right. Wave propagation is slowed down by the basin with low velocity in the area A at time 28 sec. Basin amplification is observed in area B (time 38 sec) and C (time 43 sec), where the largest velocities of the whole study area coincide with the edge of the basin.

In Fig. 7 we show some velocity seismograms excited by two hypocenters H1 and H2 (Fig. 3 inlet) on the profile AB (Fig. 4) for different components. The corresponding epicenters are marked as E1 and E2 and shown in Fig. 4 to illustrate the relative position to the profile location. The profile is across the fault trace at $y=19.0$ km and also across both the major and the small sedimentary basins of the study area. In the region C, for the y-component (perpendicular to the fault), the hypocenter H1 (about 20 km of fault distance from the profile) leads to larger velocities than H2 (about 5 km of fault distance from the profile) does. For the x-component, in the region C, H2

leads to much larger velocities than H1 does. At this time, the fact that there is a slip asperity right between H2 and the profile should not be neglected. Finally, we focus on region D (Fig. 7). H2 leads to larger velocities for the two horizontal components. To sum up, velocity components will receive different contributions from various source effects (e.g., directivity and elevation by high slip). What can be concluded is that the fault-perpendicular component is dominated by the directivity effect which explains why H1 leads to larger velocities although it is much further from the high slip asperity.

Comparison with attenuation relationship:

As a first step we compare the results from all 24 synthesized scenarios to attenuation relationship between the acceleration response spectrum (PSA) and the fault distance which is developed and widely used for the southern California region (Campbell and Bozorgnia, 2003). We compare the acceleration response spectra (PSA) at period of 4.0 sec, considering that the seismograms are low-pass filtered at period of 2.0 sec which is imposed by the threshold frequency of the finite difference method to avoid numerical dispersion.

The comparison is shown in Fig. 8 for different components, i.e., horizontal average and vertical components. First, the mean value of our results fits well with that predicted by the attenuation relationship at all distance ranges for the horizontal average component and the vertical component. Secondly, the PSA from our simulations saturate at short distances (<3 km) from the fault plane. Thirdly, for the horizontal average component, there are obviously high PSAs in the fault distance range A (Fig. 8). This fault distance range, referring to one of the subfigure in Fig 9, includes the small basin where basin amplification is observed in terms of the maximum ground velocity. The one predicted by the empirical relation, however, decreases smoothly in this range.

Ground motion properties: Hypocentre location variation

Two examples of the resulting PGVs in the LA basin are shown in Fig. 9a, 9b for the hypocentre locations H1 (5 km depth, located at SE fault edge) and H2 (15 km depth, located towards the centre) as indicated in Fig. 3 (inlet). The shallow hypocentre with unilateral rupture propagation (H1, Fig. 9a) leads to a directivity-dominated distribution of PGVs towards the NW end of the fault, while the PGVs of the bilaterally propagating rupture from the deeper hypocentre (H2, Fig. 9b) show a clear distance dependence from the fault with dominant PGVs in the NW part. This is due to the main slip occurring in the northern part of the fault (see Fig. 3, inlet). However, it is important to note that the deeper hypocentre illuminates the entire basin leading to considerably more basin-wide shaking compared to the shallower hypocentre.

The parameter study in the hypocentre space allows us to extract the PGVs of all 24 simulations (Fig. 9c) containing the dominant features of the previously shown two examples with basin wide shaking, fault-distance dependent ground motion, and peak motions above the fault area with the largest slip (asperity). The variations of the hypocentre-dependent ground motions can be expressed by relating the variance of the PGVs to the mean PGV at each point of the surface grid (Fig. 9d). The resulting distribution illustrates the regions in which most variations of ground motions are to be expected from the hypocentre location. These variations are symmetric around the fault edges with some amplification from the basin edges particularly on the SE end. The symmetry of large variation is explained with the different ground motion variation due to the directivity effect (see Fig. 5d for a velocity profile). The large variations of peak ground velocity at regions off the two tips of the fault trace are also observed in Gallovic and Brokešová (2007b) for a homogeneous model whose frequency range is

much higher than ours. It is interesting to note that - except at the fault edges - the variations are considerably larger at the small basin edge (neighbouring station R1).

The ratio between the maximum PGV and the mean PGV is also shown for the entire study area. This parameter somehow represents the worst case scenario (largest deviation from the mean) from an earthquake engineering point of view. First, for the x-component (Fig. 10 top left), the largest ratio is observed in region A where the basin depth changes fast. Also elevated ratios are observed in region B compared to the neighboring regions. Secondly, for the y-component (Fig. 10 top right), large ratios are observed in region C and D. These two regions are aligned with almost equal angle to the fault trace. In region D, even outside the basin, there are still high ratios. Thirdly, for the z-component, large ratios are distributed, more evenly on the entire study area than those for the other two components. The largest ratio happens inside region E where high basin depth gradients exist.

We complete this study by investigating the relationship between PGV and hypocentre depth for all simulated scenarios and two receivers indicated in Fig. 9 (R1, 40 km from the fault, inside the basin; R2, above the centre of the fault). Horizontal velocity seismograms (fault-parallel component) are shown for receivers R1, R2 and four different hypocentral depths (same epicentre) as indicated in Fig. 3 (inlet, white rectangle). The PGVs (and variance) for all 24 simulations at receivers R1, R2 are displayed as a function of source depth in Fig. 11c, 11d, respectively. For the distant receiver (R1, Fig. 11c) the mean PGV increases slightly with source depth, while the variance is much larger for deeper events, indicating a stronger path-dependence for wave fields arriving from deep sources than from shallow sources. The opposite behaviour is observed for receiver R2 close to the fault (Fig. 11d). Due to geometrical spreading, more effects due to 3D structure are observed for ground motions recorded

at R1 (far from the fault) and more effects due to the source process are expected for R2 (close to the fault).

5. Conclusions

We have introduced the concept of numerical Green's functions (NGF) that can be applied to discretized faults or fault systems in 3D media allowing the calculation of earthquake scenarios from arbitrary slip histories. NGF data bases allow a systematic study of source related uncertainties/variations of seismic hazard relevant wave field properties (peak ground motions, static displacements and rotations, shaking duration, etc.) varying slip distributions (e.g., asperity locations), slip and rupture velocities, hypocentre locations, etc. Particularly interesting is the possibility to apply high-resolution slip histories from dynamic rupture simulations and investigate their relevance to shaking hazard.

Our simple example on the influence of hypocentre location on the resulting ground motions indicates complex behaviour with dependence of PGV distribution and its variation on asperity location, directionality and local structure. The high slip asperity will lead to large velocities in its neighbouring regions. Large velocities and variations are observed close to the basin edge. Different variations are observed between different components. The fault perpendicular component is dominated by the directivity effect due to its transverse position when considering the S-wave radiation pattern from a double couple point source. We compare our ground motions with those predicted with attenuation relationships as a function of fault distance and illustrate the amplification of the medium on the ground motions. In addition, hypocentral depth may

affect PGV in a positive or negative way, depending on the distance from the fault, and location with respect to basin structure.

This study was subject to severe limitations. Amongst others, (1) the fault is approximated by a vertical plane and pure strike-slip source mechanism. (2) The lowest shear-velocity (1.4 km/s) is too high to be useful for realistic hazard estimates and the highest frequencies are only relevant for very tall buildings. (3) We limited ourselves to investigate only one M7 earthquake happening on the same fault with the same final slip distribution. Yet, the main purpose of this study is to illustrate the potential functionalities of an NGF data base and the possibilities to systematically investigate source related uncertainties in 3D areas with high seismic hazard. Source related uncertainty in 3D media is an issue that has so far not been addressed properly, partly due to limitations of computational resources. It is important to note that such NGF data bases only make sense if the crustal structure is sufficiently well known and that the NGF data base would need to be recalculated with every model update (it might be possible to devise approximate updates of the NGF data base). Nevertheless, we suggest that this methodology may be useful also on a larger scale particularly for mega-faults in subduction zones with tsunami-generating potential.

Acknowledgements

This work was partially funded by the International Quality Network - Georisk (German Academic Exchange Service), and the Elite Graduate College THESIS (elite.geophysik.uni-muenchen.de). We also acknowledge support from the European Human Resources Mobility Programme (Research Training Network SPICE, www.spice-rtn.org) and the provision of computational resources through the Leibniz Computing Centre Munich. ME was partly funded by the KONWIHR project and a stipend of the MunichRe.

References

- Aki, K., and P. G. Richards (2002), *Quantitative seismology*, 2nd Edition, University Science Books.
- Beresnev, I. A., G. M. Atkinson, P. A. Johnson, and E. H. Field (1998), Stochastic finite-fault modelling of ground motions from the 1994 Northridge, California, earthquake. II. Widespread nonlinear response at soil sites, *Bull. Seism. Soc. Am.*, **88**, 1402-1410.
- Boore, D. M. (2003), Simulation of ground motion using the stochastic method, *Pure and Applied Geophysics*, **160**, 635-676.
- Bour, M., and M. Cara (1997), Test of simple empirical green's functions method on moderate-sized earthquakes, *Bull. Seism. Soc. Am.*, **87**, 668-683.
- Campbell, K. W., and Y. Bozorgnia (2003), Updated near-source ground-motion (attenuation) relations for the horizontal and vertical components of peak ground acceleration and acceleration response spectra, *Bull. Seism. Soc. Am.*, **93**, 314-331.
- Collino, F., and C. Tsogka (2001), Application of the PML absorbing layer model to the linear elastodynamic problem in anisotropic heterogeneous media, *Geophysics*, **66**, 294-307.
- Ewald, M., H. Igel, K. G. Hinzen, and F. Scherbaum (2006), Basin-related effects on ground motion for earthquake scenarios in the Lower Rhine Embayment, *Geophys. J. Int.*, **166**, 197-212.
- Gallovic, F. and J. Brokešová (2004), The k^2 rupture model parametric study: example of the 1999 Athens earthquake, *Studia geoph. et geod.*, **48**, 589-613.
- Gallovic, F. and J. Brokešová (2007a), Hybrid k -squared Source Model for Strong Ground Motion Simulations: Introduction. *Phys. Earth Planet. Interiors*, **160**, 34–50.

- Gallovic, F. and J. Brokešová (2007b). Probabilistic Aftershock Hazard Assessment II: Application of Strong Ground Motion Modeling. *submitted to J. Seismology*.
- Gerstenberger, M. C., S. Wiemer, L. M. Jones, and P. A. Reasenber (2005), Real-time forecasts of tomorrow's earthquakes in California, *Nature*, **435**, 328-331.
- Gottschämmer, E., and K. B. Olsen (2001), Accuracy of explicit planar free-surface boundary condition implemented in a fourth-order staggered-grid velocity-stress finite-difference scheme, *Bull. Seism. Soc. Am.*, **91**, 617-623.
- Grant, L. B., and P. M. Shearer (2004), Activity of the offshore Newport - Inglewood Rose Canyon fault zone, coastal Southern California, from relocated microseismicity, *Bull. Seism. Soc. Am.*, **94**, 747-752.
- Graves, R. W., and D. J. Wald (2001), Resolution analysis of finite-fault source inversion using one- and three-dimensional Green's functions 1. Strong motions, *J. Geophys. Res.*, **106**, 8745-8766
- Guatteri, M., P. M. Mai, and G. C. Beroza (2004), A pseudo-dynamic approximation to dynamic rupture models for strong ground motion prediction, *Bull. Seism. Soc. Am.*, **94**, 2051-2063.
- Hauksson, E., and S. Gross (1991), Source parameters of the 1933 Long Beach earthquake, *Bull. Seism. Soc. Am.*, **81**, 81-98.
- Hu, Y. X., S. C. Liu and W. M. Dong (1996), Earthquake Engineering, E & FN SPON
- Hutchings, L., and F. Wu (1990), Empirical Green's functions from small earthquakes - a waveform study of locally recorded aftershocks of the San Fernando earthquake, *J. Geophys. Res.*, **95**, 1187-1214.
- Igel, H., P. Mora and B. Riollot (1995), Anisotropic wave propagation through finite-difference grids, *Geophysics*, **60**, 1203-1216.
- Jennings, C. W. (1994), Fault activity map of California and adjacent Areas with location and ages of recent volcanic eruptions. *California Geologic Data Map Series*, Map No. **6**. California Division of Mines and Geology.

- Joyner, W. B. and D. M. Boore (1986), On simulating large earthquakes by Green's-function addition of smaller earthquakes. *Earthquake Source Mechanics*, Geophysical Monograph No. 37 (Maurice Ewing, ed.), **8**, 269-274.
- Kanamori, H. (1977), The energy release in great earthquakes, *J. Geophys. Res.*, **82**, 2981-2987.
- Kohler, M., H. Magistrale, and R. Clayton (2003), Mantle heterogeneities and the SCEC three-dimensional seismic velocity model version 3, *Bull. Seism. Soc. Am.*, **93**, 757-774.
- Kohrs-Sansorny, C., F. Courboux, M. Bour, and A. Deschamps (2005), A Two-stage method for ground-motion simulation using stochastic summation of small earthquakes, *Bull. Seism. Soc. Am.*, **95**, 1387-1400.
- Mai, P. M., and G. C. Beroza (2002). A spatial random-field model to characterize complexity in earthquake slip, *J. Geophys. Res.*, **107**(B11), 2308, doi: 10.1029/2001JB000588, 2002.
- Marcinkovich, C., and K. B. Olsen (2003), On the implementation of Perfectly Matched Layers in a 3D fourth-order velocity-stress finite-difference scheme, *J. Geophys. Res.*, **108**, 2276-2293.
- Olsen, K. B. (2000), Site amplification in the Los Angeles basin from 3D modelling of ground motion, *Bull. Seism. Soc. Am.*, **90**, S77-S94.
- Olsen, K. B. and R. J. Archuleta (1996), 3D-simulation of earthquakes in the Los Angeles fault system, *Bull. Seism. Soc. Am.*, **86**, 575-596.
- Wang, H. J. (2007), Source-dependent variations of M7 earthquakes in the Los Angeles basin, Doctoral thesis, Ludwig-Maximilians-University Munich.

Table 1: Verification setup for the homogeneous case

Spatial discretization (m)	1000
Time step (s)	0.0822
S-wave velocity (m/s)	3900.0
P-wave velocity (m/s)	6754.8
Density (kg/m ³)	2811.0
Simulation time (s)	50
Study area (km)	120×130×45
PML Nodes padded	15
Constant slip rate (m/s)	2.9

Table 2: Verification setup for the heterogeneous model in the Los Angeles basin

Spatial discretization (km)	0.3
Time step (s)	0.018
Lowest S-wave velocity (km/s)	1.4
Simulation time (s)	65
Number of cells	320×350×100
PML Nodes	15
Fault area (km ²)	18×36
Top depth (km)	1.5

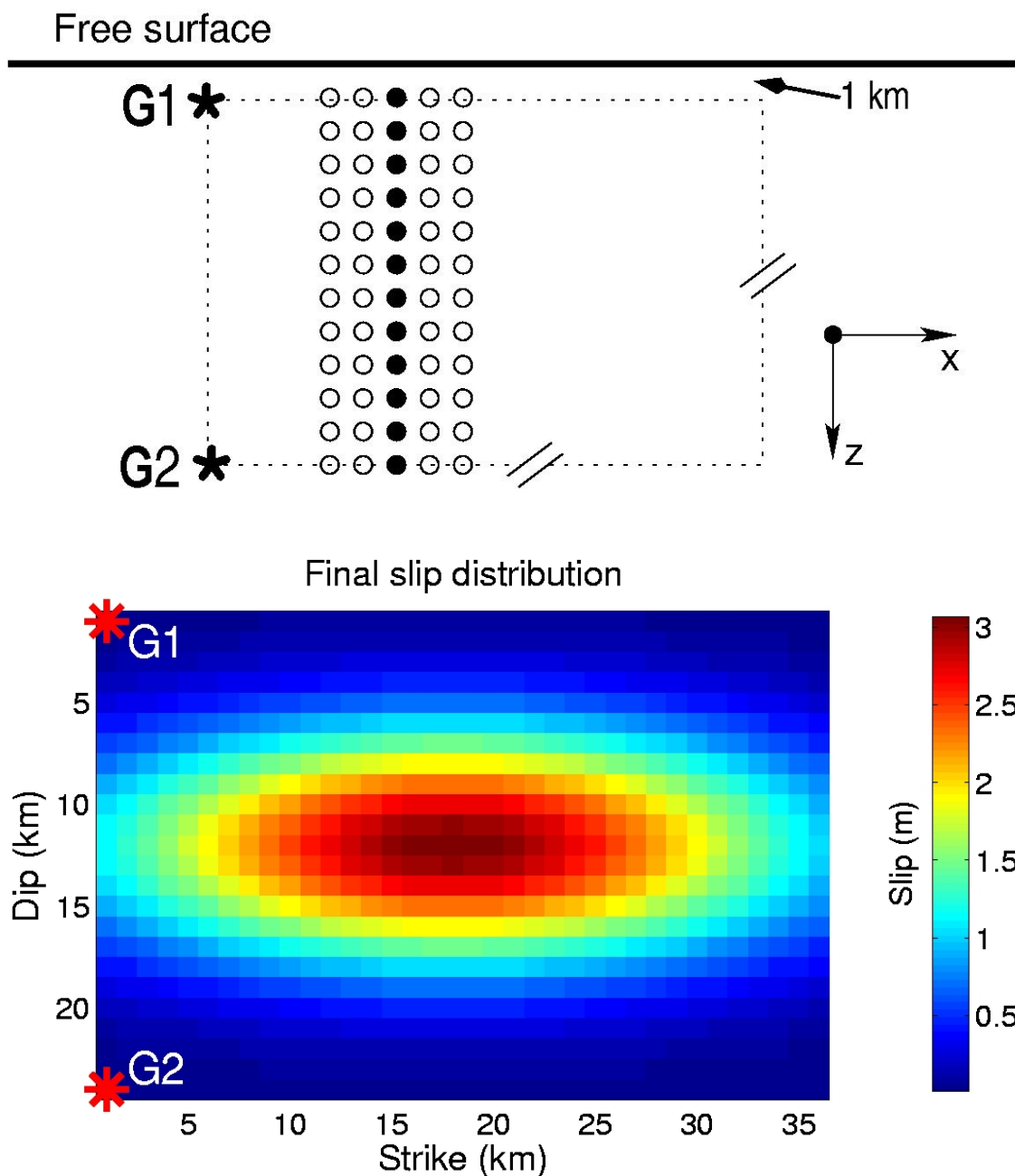


Figure 1: Top. Schematic set-up for the homogeneous case. The thick black line is the free surface. Black solid circles are the hypocentres of a set of double-couple point sources and the big asterisks mark the fixed hypocentres for an earthquake whose fault plane is represented by the thin dashed rectangle (which is uniformly discretized and represented with cycles, solid and open). **Bottom.** Final slip distribution calculated for an Mw 7.0 earthquake (see Mai and Beroza 2002) with two hypocentres, G1 and G2.

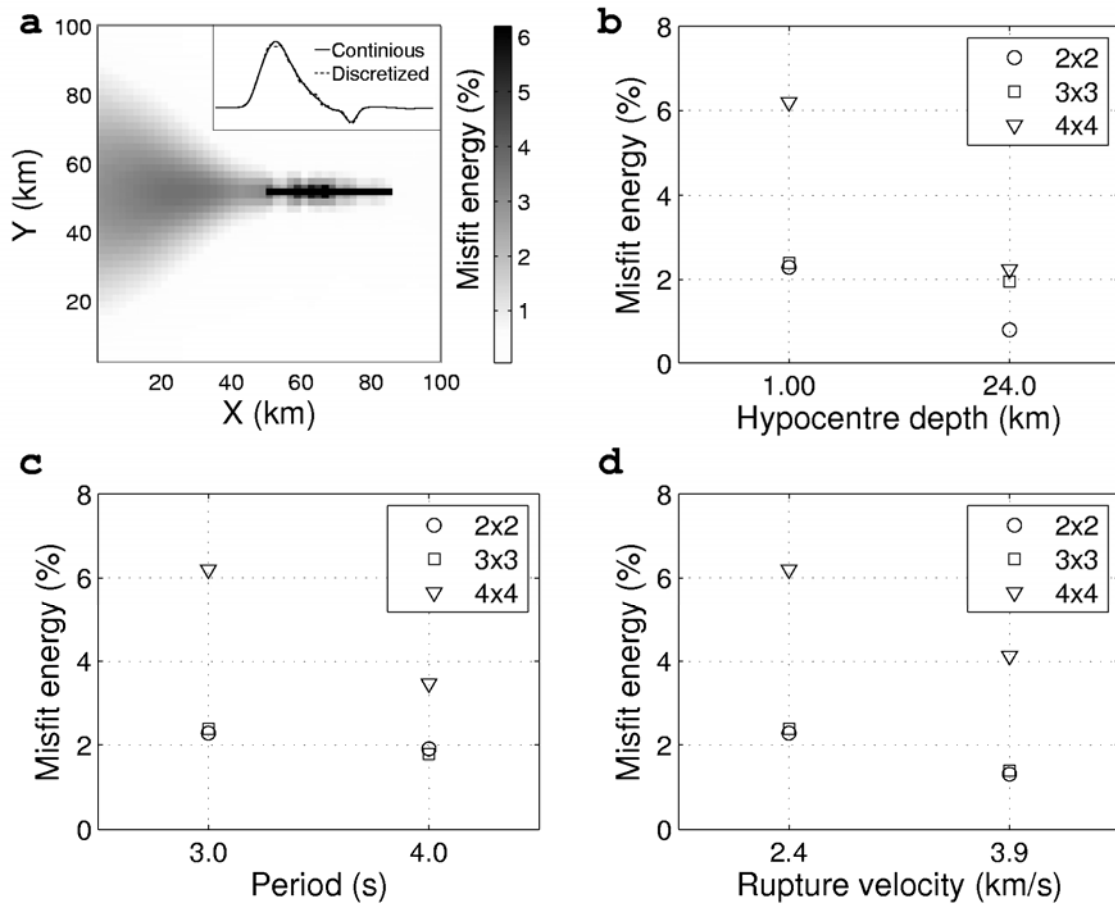


Figure 2: Accuracy of seismogram synthesis as a function of sub-fault size, hypocentre depth, frequency range and rupture velocity. **a.** Misfit energy (ME) (%) (see definition in equation (3)) at each surface grid between sub-fault size 4.0×4.0 km and “continuous” solution (1.0×1.0 km). In the inlet two velocity seismograms are shown. Thick black line (36 km in length) marks the M7 earthquake fault trace. **b.** ME as a function of hypocenter depth. **c.** ME as a function of cut-off period (Gaussian low-pass filtering). **d.** ME as a function of rupture velocity. x-component of velocity is used in this figure for the reason that it is the least accurate.

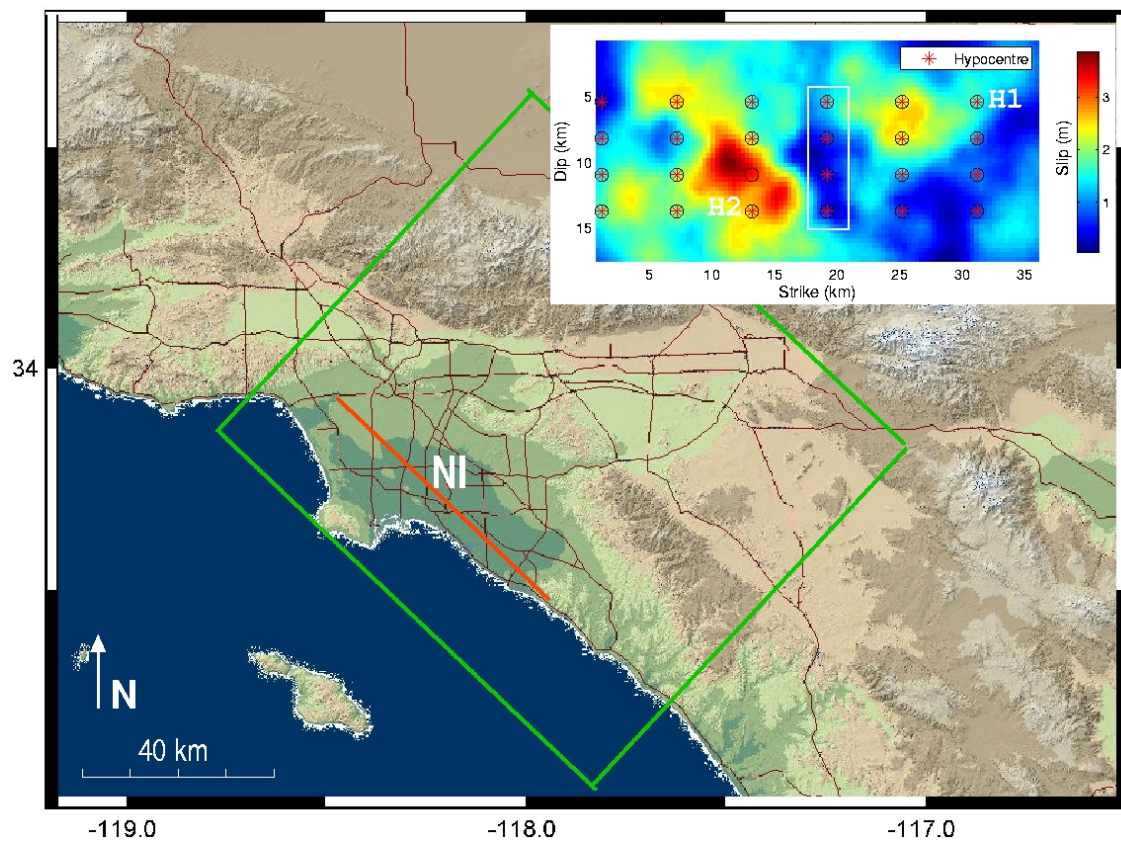


Figure 3: Los Angeles area with modelled region (green rectangle) and the idealized Newport-Inglewood fault (NI, red line). Inlet: Final slip distribution of an M7 earthquake on the vertical NI fault plane and hypocentre grid (red asterisks, for investigation of hypocentral effect on ground motion). H1 and H2 show the two example hypocentre locations for more detailed exhibition of hypocentral effect on ground motion.

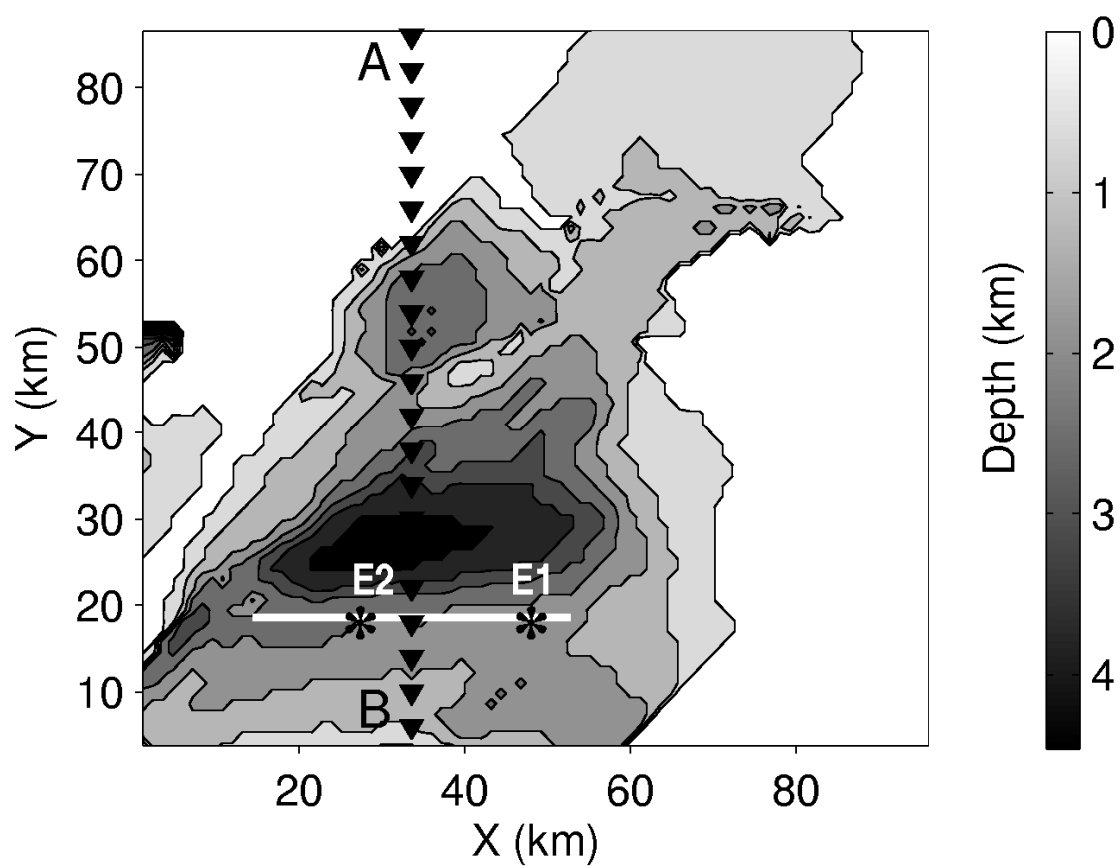


Figure 4: Depth of shear wave velocity isosurface at 2.0 km/s (grey scale). The thick white line marks the fault trace of the M7 earthquake. Profile AB (black solid triangle) is used for detailed discussion. E1 and E2 are the epicentres corresponding to hypocentre H1 and H2 (Fig. 3 inlet).

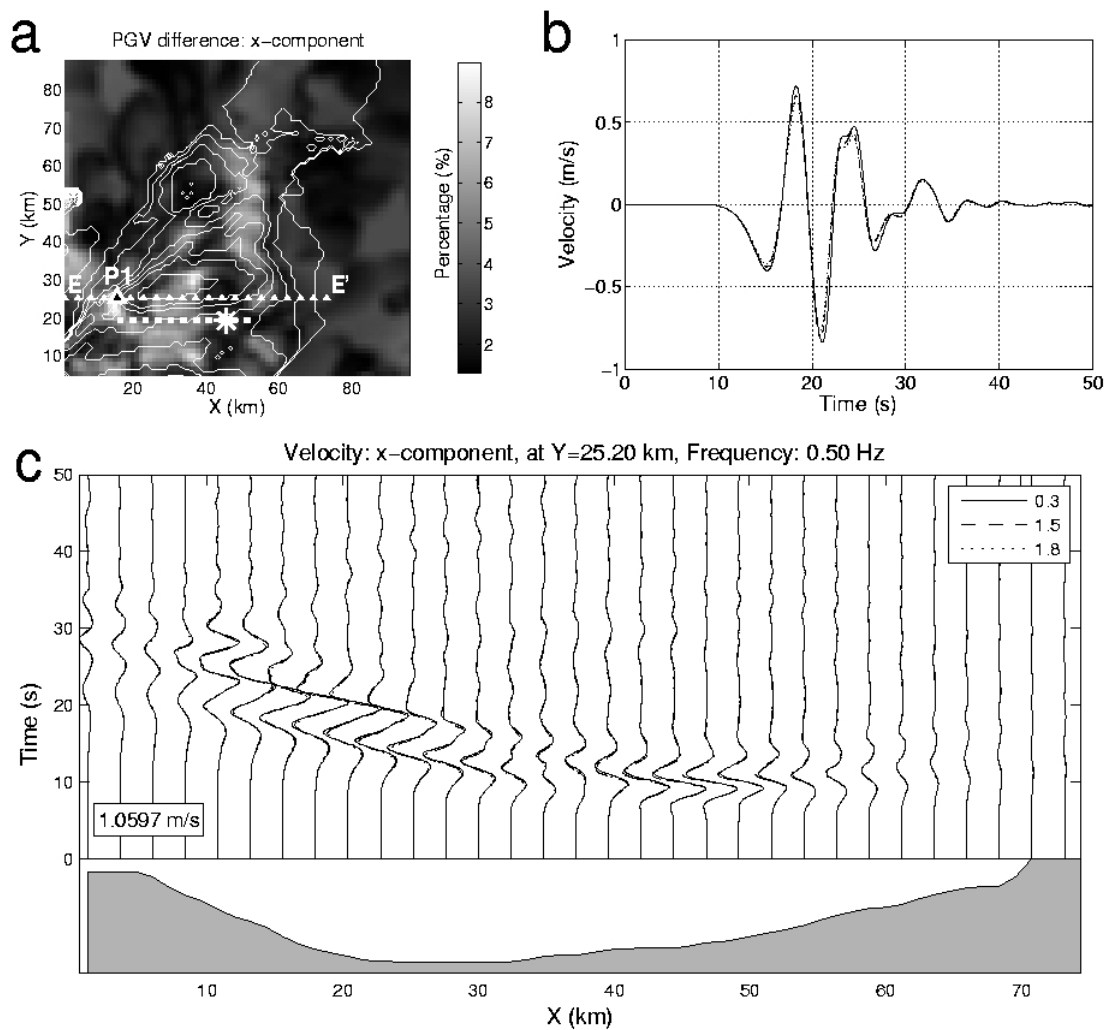


Figure 5: Optimal sub-fault size determination for an M7 earthquake in LA basin. **a.** Relative PGV difference distribution (see definition in text) between the discretized solution of 1.8 km and the “continuous” solution where dashed thick white line marks the fault trace and the big asterisk, the epicentre. The biggest relative PGV difference is observed at station P1. **b.** Velocity seismograms of differently discretized solutions, i.e., 0.3 km, 1.5 km and 1.8 km, respectively, for station P1 in **a.** **c.** Velocity profile, EE’ (**a**), of differently discretized solutions. The maximum velocity amplitude on this profile is shown with the inlet number. The grey area at the bottom shows the isosurface depth of shear wave velocity at 2 km/s.

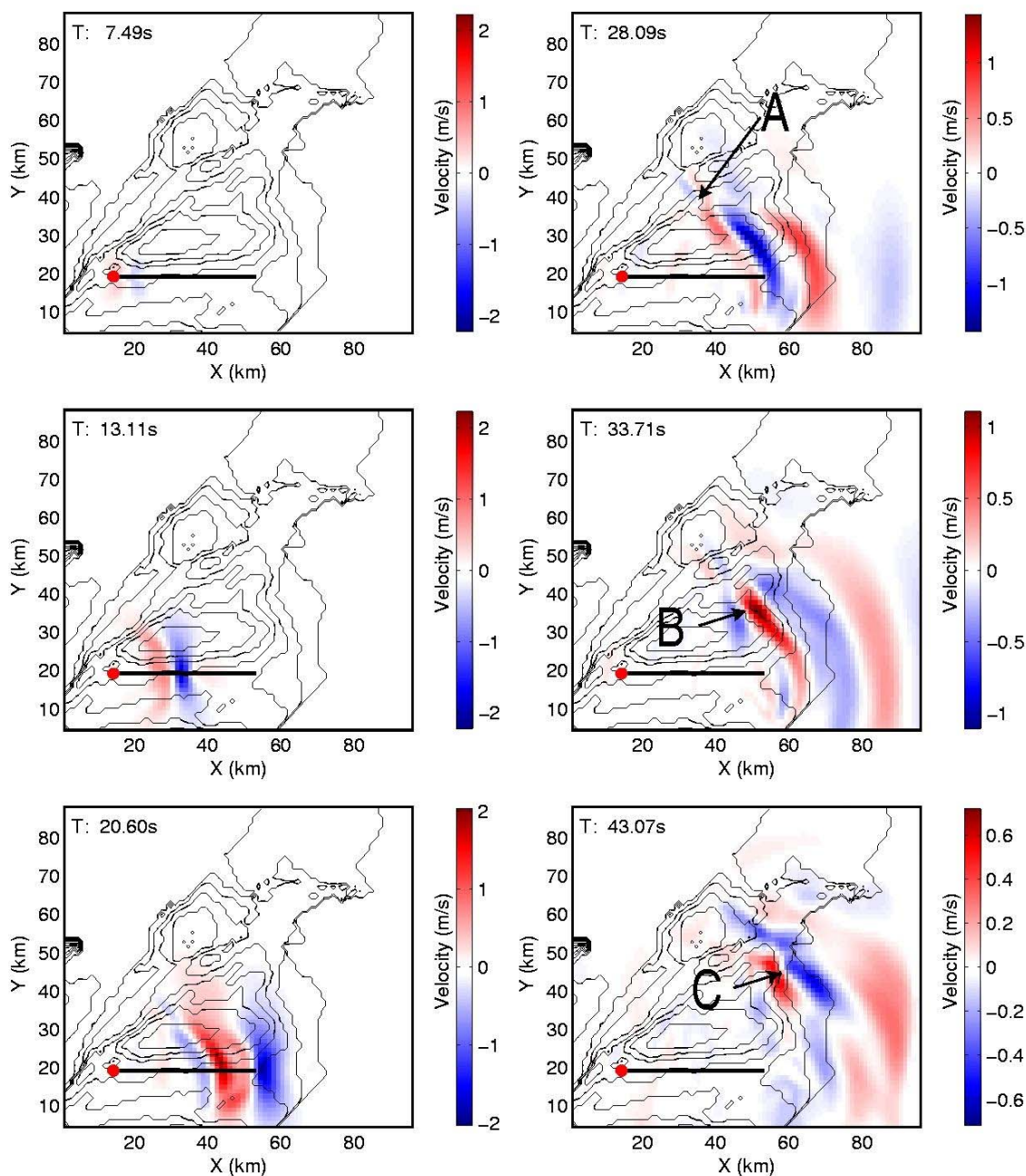


Figure 6: Velocity snapshots of y-component at different times (Hypocentre is shown as red solid circle with depth of 7.6 km from the surface). Black thin lines show the contours of isosurface of shear wave velocity at 2 km/s. Thick black line shows the fault trace. Areas A, B and C are depicted to illustrate the structure effect on wave propagation. Note the change of the color scale.

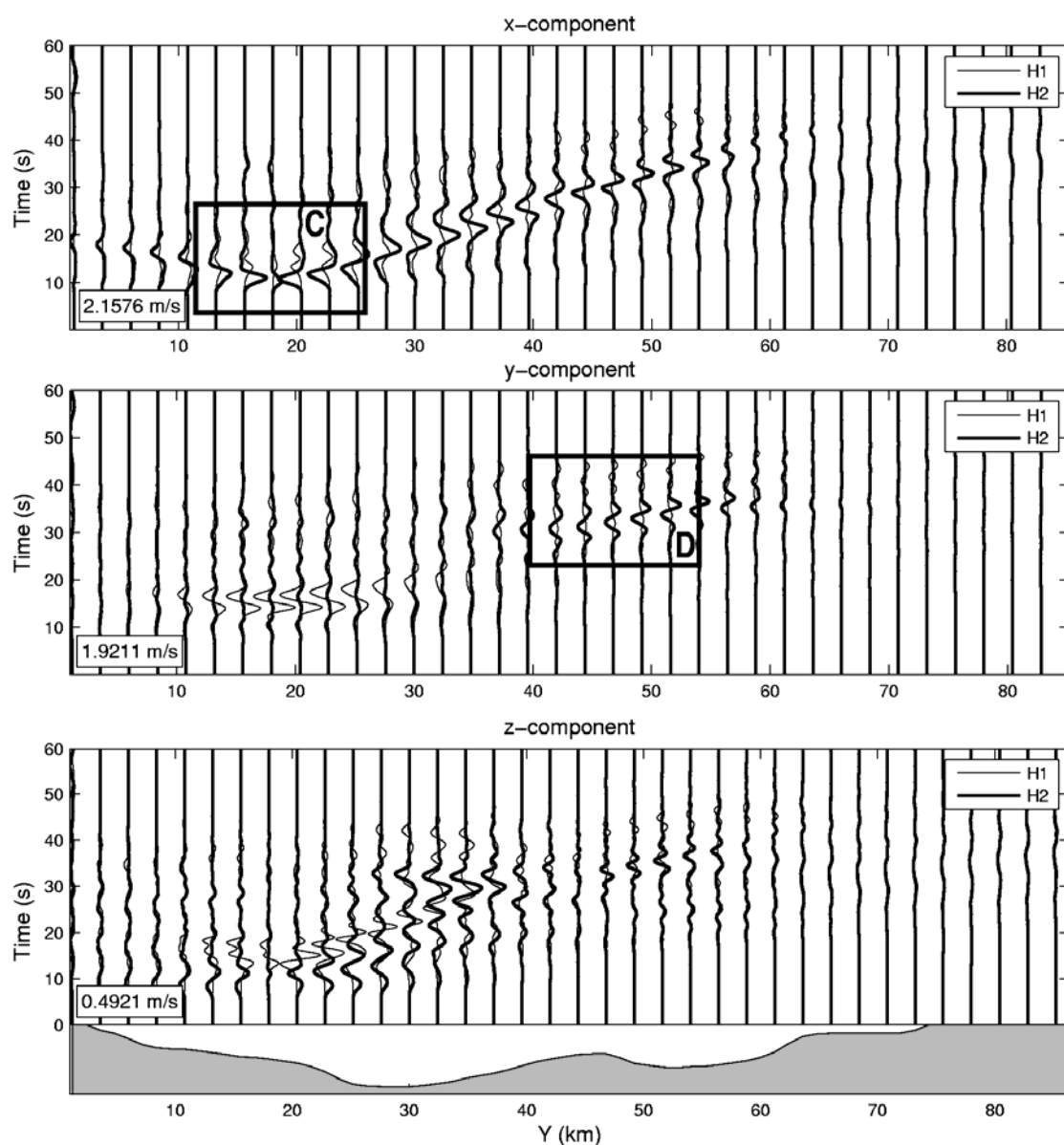


Figure 7: Velocity profile (Fig. 4 AB) simulated with two example hypocenter H1 and H2 (Fig. 3 inlet, the corresponding epicenters E1 and E2 are shown in Fig. 4 as black asterisk). From top to bottom are the x-, y- and z-components, respectively. The shear wave velocity isosurface depth (at 2.0 km/s) is depicted in the bottom as the shadowed area. The maximum velocity amplitude across this profile is shown with the inlet number.

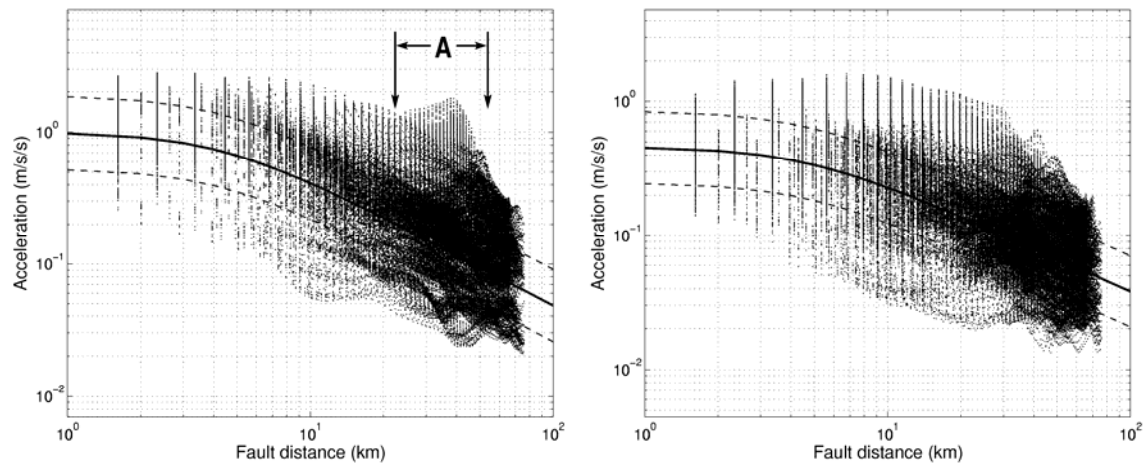


Figure 8: Comparison with the attenuation relation (Campbell and Bozorgnia, 2003). **Left.** Horizontal average component. **Right.** z-component. Each dot represents the peak acceleration response (PSA) value at a station whose fault distance is shown in the x-axis. The empirical PSA's attenuation with the fault distance is depicted with thick black line with log-normal standard deviation (thin dashed line) at by-sides. Region A is picked up for deeper discussion.

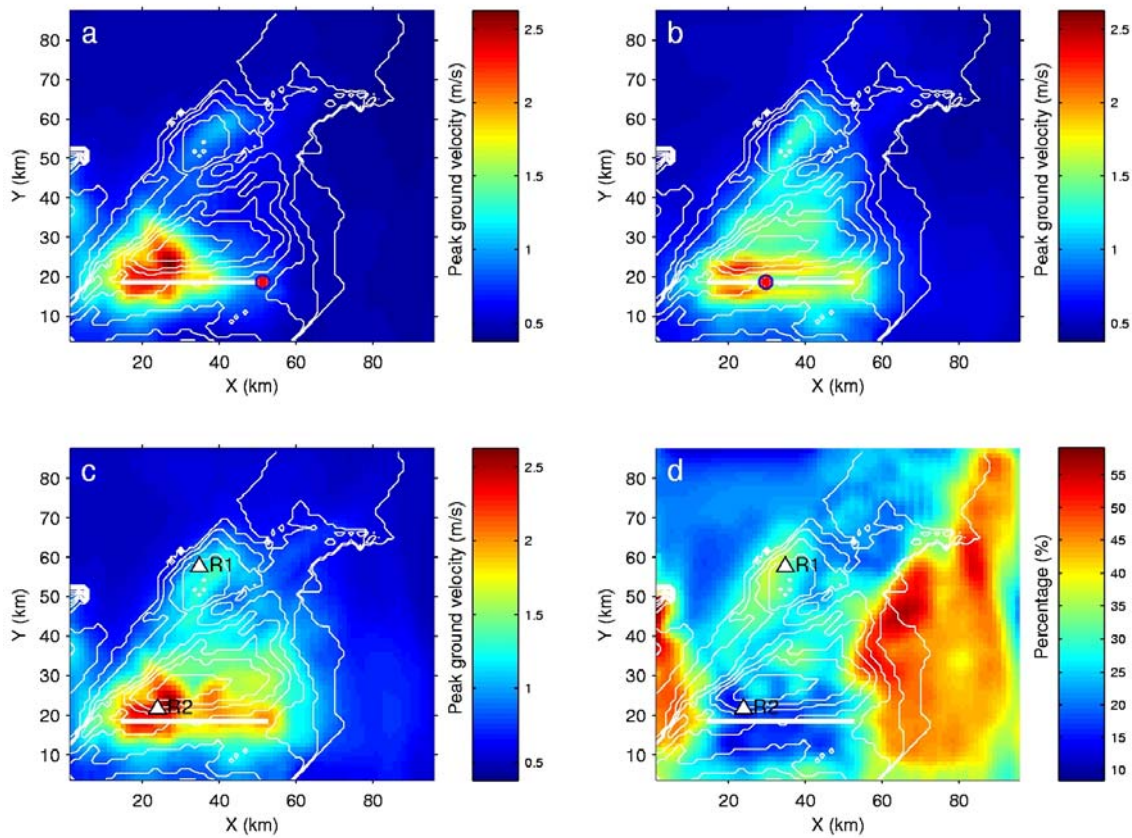


Figure 9: **a.** Peak ground velocity (PGV, modulus of horizontal components) for hypocentre H1 (Fig. 3 inlet). **b.** Same for H2 (Fig. 3 inlet). The epicentres are indicated as red solid cycles. The straight white line indicates the fault trace. Thin white lines are contours of the seismic velocity model. **c.** Maximum of PGVs for the combination of all 24 simulations. **d.** The ratio between the standard deviation and the mean PGV value (combination of all 24 simulations, too) in percent. R1 and R2 are the two example positions chosen to show more detailed results.

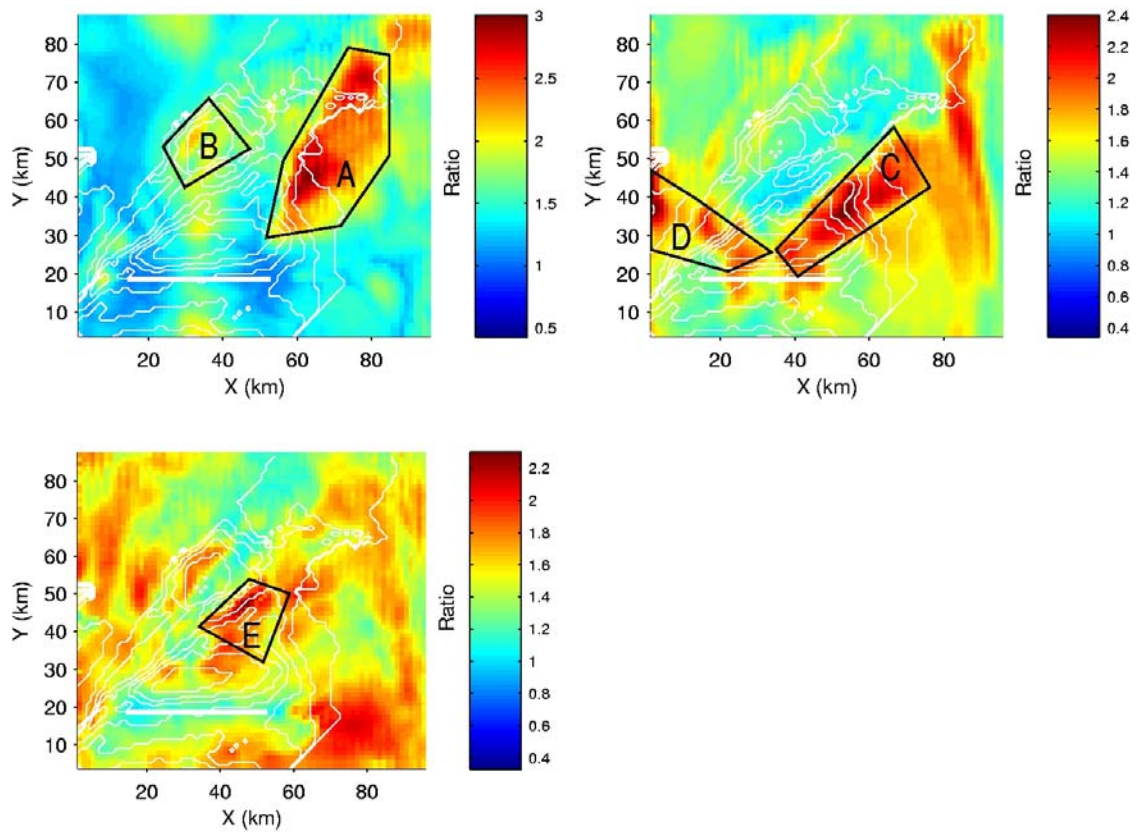


Figure 10: The ratio between the maximum and the mean PGV. **Top left.** x-component. **Top right.** y-component. **Bottom left.** z-component. The white line indicates the fault trace. Thin white lines are contours of the seismic velocity model. Region A, B, C, D and E are picked up for more detailed discussion. Note the color scale difference.

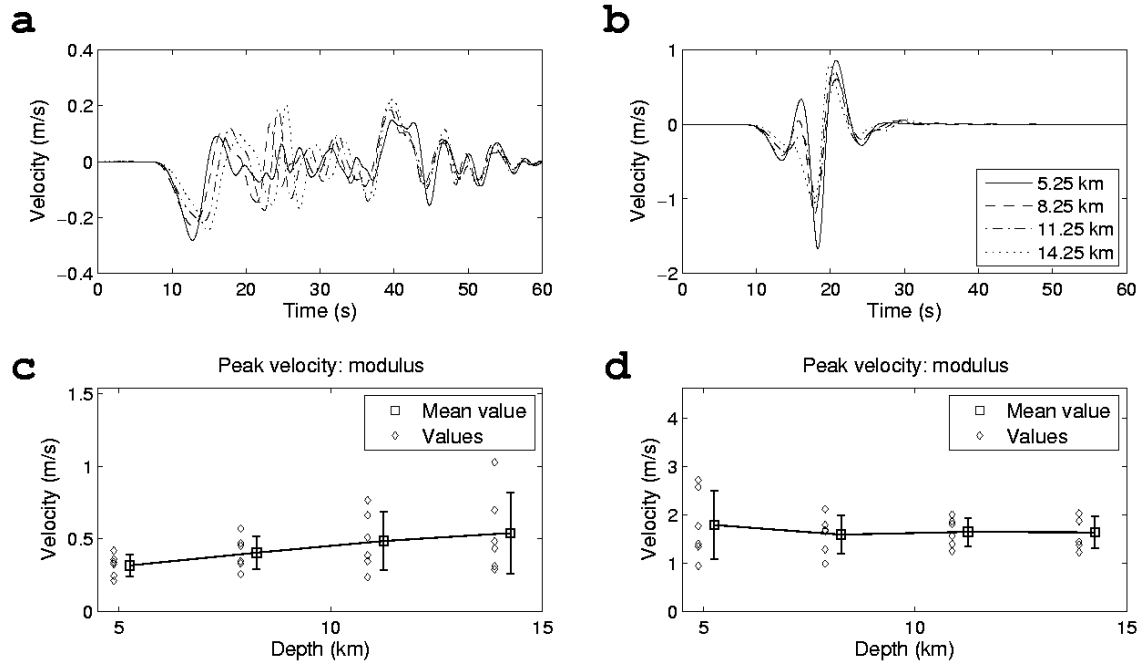


Figure 11: a+b: Velocity seismograms (x-component) for the M7 earthquake with same epicentre but varying source depth (see Fig. 3, inlet, white rectangle) at receivers indicated in Fig. 9c. **a.** R1, approx. 40 km off fault. **b.** R2, close to the fault trace. **c+d:** PGV as well as mean and variance for all simulations. **c.** R1; **d.** R2. Mean value and variances are offset for illustrative reasons.